



HAL
open science

Experimental (TEM and STEM) investigation and theoretical approach to the fatigue-induced dissolution of delta'-precipitates in a 2.5 wt % Al-Li alloy

Yves Brechet, François Louchet, C. Marchionni, J.-L. Verger-Gaugry

► To cite this version:

Yves Brechet, François Louchet, C. Marchionni, J.-L. Verger-Gaugry. Experimental (TEM and STEM) investigation and theoretical approach to the fatigue-induced dissolution of delta'-precipitates in a 2.5 wt % Al-Li alloy. Philosophical Magazine a, 1987, 56 (3), pp.353-366. 10.1080/01418618708214391 . hal-03134559

HAL Id: hal-03134559

<https://hal.science/hal-03134559>

Submitted on 11 Feb 2021

HAL is a multi-disciplinary open access archive for the deposit and dissemination of scientific research documents, whether they are published or not. The documents may come from teaching and research institutions in France or abroad, or from public or private research centers.

L'archive ouverte pluridisciplinaire **HAL**, est destinée au dépôt et à la diffusion de documents scientifiques de niveau recherche, publiés ou non, émanant des établissements d'enseignement et de recherche français ou étrangers, des laboratoires publics ou privés.

Experimental (TEM and STEM) investigation and theoretical approach to the fatigue-induced dissolution of δ' precipitates in a 2.5 wt % Al-Li alloy

Y. Bréchet, F. Louchet, C. Marchionni and J.-L. Verger-Gaugry

LTPCM/ENSEEG/INPG (CNRS UA 29), BP 75, Domaine Universitaire, 38402 Saint Martin d'Hères, France

Abstract. The fatigue microstructure of an Al-2.5 wt %Li alloy with small precipitates has been investigated both by TEM and STEM (nanodiffraction and electron energy loss spectroscopy). Specific features of strain localization have been evidenced which are made of lithium-depleted precipitate-free bands. A model is proposed to explain the redissolution of δ' precipitates inside the bands, based on an increase of their free energy due to shear-induced antiphase boundaries.

§ 1. INTRODUCTION

Some f.c.c. crystals (Cu and Ni for example), if tested in fatigue within an appropriate range of plastic strain amplitude $\Delta\varepsilon_p$, exhibit a particular type of localized deformation structure, the so-called persistent slip bands (PSB) (for a review see Magnin, Driver, Lepinoux and Kubin 1984). These ladder-shaped structures are characterized by high-density dislocation walls of edge character bounding channels where screw dislocations can easily propagate and annihilate one another. However, in pure aluminium and in aluminium-based alloys, this kind of localized slip band is not observed whatever the strain amplitude might be, at least at room temperature (Mughrabi 1985). Instead, another type of PSB has been observed in precipitate-hardened Al alloys by Vogel, Wilhem and Gerold (1979) in Al-Zn-Mg, and by Köhler, Bischoff and Gerold (1984) in Al-Ag. In these cases, deformation gets localized into narrow bands in which ordered precipitates had disappeared. The question whether the disappearance of the precipitates comes from a disordering (Calabrese and Laird 1973) or a dissolution still remains controversial.

In aluminium-lithium binary alloys, a metastable, ordered and coherent phase, of structure L12, labelled δ' , appears for concentrations larger than about 2 wt% or 8 at.%. This precipitation leads to a localization of strain in monotonic deformation. In the case of fatigue, macroscopic instabilities are observed in the cyclic stress-strain curves (Fougères, Gentzittel and Vigier 1987, Han and Wack 1987) and this suggests the presence of an intense strain localization. Here we analyse by TEM and STEM techniques the localized microscopic structure observed on a binary 2.5 wt% aluminium alloy which exhibited the above instabilities during a fatigue test in torsion.

§ 2. EXPERIMENTAL PROCEDURE

The material used was a binary Al-2.5 wt%Li alloy provided by Cegedur Pechiney, aged for 8 h at 100°C. The resulting average radius of δ' precipitates measured by X-ray low-angle scattering was about 1 nm that is far below the critical radius for Orowan looping (Sainfort and Guyot 1985 a, Bréchet, Guyot and Louchet 1986). Hollow specimens ($\phi_{\text{int}} = 26$ mm, $\phi_{\text{ext}} = 30$ mm) were machined and fatigued to failure in the torsion mode at an imposed total deformation amplitude $\frac{1}{2}\Delta\epsilon_t = 0.3\%$ with a period $T = 8 \times 10^{-2}$ s ($\dot{\epsilon} = 10^{-3}$ s $^{-1}$).

Slices were then cut parallel to the surface of the specimens and thinned down by mechanical and electrolytic polishing in order to obtain thin foils. TEM observations were performed either in a bright field or by using dark-field superlattice reflections in order to image the ordered δ' precipitates in a JEOL 200CX microscope operating at 200 kV.

Thin foils were also observed in a Vacuum Generator HB501 scanning transmission electron microscope (STEM) equipped with a field emission gun and operating at 100 kV. The energy resolution of the incident beam was 0.4 eV. Condenser lens excitations were set up in order to allow an electron probe size on the specimen less than 1.3 nm with a virtual objective aperture of 200 μm diameter. EELS analysis was performed using a Tractor Northern TN2000 multichannel analyser. Energy-loss spectra of electrons transmitted through the foils were recorded with an energy width per channel of 0.05 eV and a maximum scattering angle of 7.6 mrad for single scattering events.

The information contained in the bulk plasmon energy position, which actually reflects the free electron density at the scale of the probe size, was used to obtain filtered images and to perform local analysis. Indeed, the estimation of lithium concentration C was achieved by measuring the lateral shift of the plasmon peak induced by the presence of Li, from the experimental reference value 15.09 eV for pure Al, and by calculating C from the linear relation demonstrated by Sainfort (Sainfort and Guyot 1985 b) in binary Al-Li alloys. The experimental plasmon energy loss ΔE is given by

$$\Delta E \text{ (eV)} = 15.09 - 3.97C_{\text{Li}} \text{ (at. \%)} \quad (1)$$

Filtered images were obtained by selecting electrons that had lost a definite amount of energy ΔE within an energy window of 0.1 eV.

The noise of the images was eliminated using an image analyser IBAS of Kontron which works on pictures of 512×512 pixels and 256 grey levels. Taking advantage of the directional character of the information contained in the images, we eliminated the noise with a large, linear, low-pass filter parallel to the slip bands. We also improved the grey-level dynamics with a shading correction and a constant reinforcement.

§ 3. EXPERIMENTAL RESULTS

3.1. TEM observations

Figure 1 shows a diffraction pattern obtained with an electron beam parallel to a $[\bar{1}12]$ direction. Superlattice reflections clearly demonstrate the presence of the δ' phase. Observations in the imaging mode were performed using a $[1\bar{1}1]$ reflection in a bright field and a $[\bar{1}10]$ superlattice reflection in a dark field (figs. 1(a) and (b)).

These pictures show narrow channels parallel to $(1\bar{1}1)$ slip planes with a width of about 5 nm. In fig. 1(b), δ' precipitates with a radius of about 1.5 nm (as measured

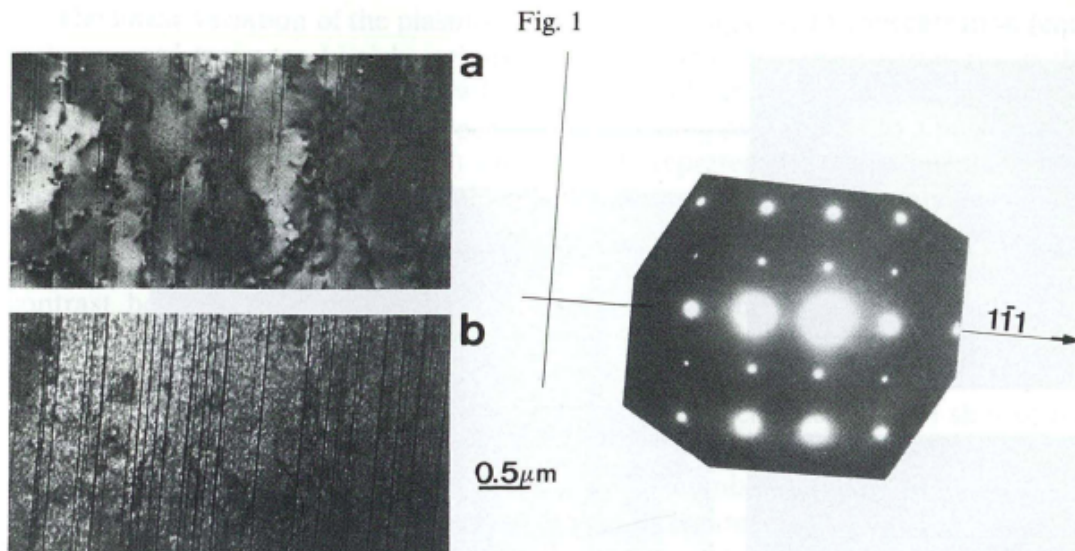


Fig. 1
 (a) Bright-field and (b) superlattice reflection images of precipitate-free bands (PFB) in TEM. The diffraction pattern shows that the bands are parallel to $\{111\}$ slip planes.

after fatigue by low-angle X-ray scattering) are clearly visible between channels but have completely disappeared inside the channels. Conversely, a strong increase of the size and the volume fraction of precipitates δ' is observed on both sides of the channels (the 'snow plough effect').

It must be noticed that to observe these precipitate-free bands (PFB) an accurate orientation of the specimen is necessary. A misorientation $\Delta\theta$ larger than d/t , where d is the PFB's width and t the thickness of the specimen, would lead to an overlap of the images of the 'snow drifts' and the images of the channels would vanish. In our case, $d \simeq 5$ nm and $t \simeq 200$ nm lead to $\Delta\theta \simeq 2.5 \times 10^{-2}$ rad.

3.2. STEM observations

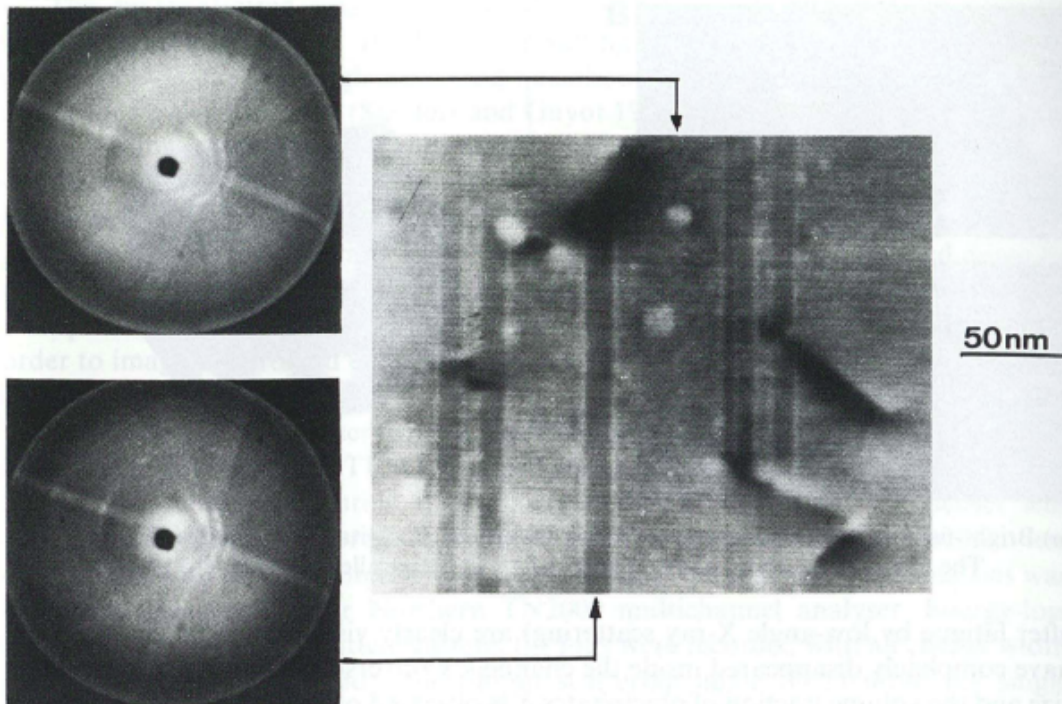
3.2.1. Band misorientations by nanodiffraction

When the matrix is orientated with the axis $[\bar{1}12]$ parallel to the electron beam, bands observed in the TEM (fig. 1) are very contrasted in bright and dark fields. This suggests that the contrast arises either from a slight misorientation of the whole band with respect to the matrix or from a different chemical composition.

Because of the small widths of bands (3 to 10 nm), nanodiffraction in the STEM was particularly well adapted to test whether some misorientation of the bands occurs, with respect to the matrix, owing to the fine scale of the probe size around 1 nm. To improve the accuracy of the misorientation measurement, regions of medium thickness were investigated, for which pairs of Kikuchi lines of the matrix were clearly contrasted on the nanodiffraction pattern. The STEM was operated in the normal imaging mode, even for nanodiffraction, with the help of a removable diffraction screen drilled in the centre which allowed simultaneous display on a TV monitor of the nanodiffraction pattern deprived of its central spot and the corresponding bright-field image on the usual TV screen of the STEM.

In order to image bands in bright field, the zone axis $[112]$ was chosen and the specimen orientated by following Kikuchi pairs on Kikuchi maps. A very slow motion of the probe across several bands, at a high magnification (above 500 000), was then

Fig. 2



STEM bright-field image of precipitate-free bands. Two nanodiffraction patterns have been taken inside and outside the bands (arrows) and show no misorientation.

performed. It resulted in no shift of the Kikuchi pattern at all, in any direction. Figure 2 shows two Kikuchi patterns associated with the matrix and with the inner part of a band. The Kikuchi pattern of the interfacial region between the band and the matrix is also identical. If a misorientation effectively occurs, the sensitivity of this method shows that it should be negligible compared with the Bragg angles, and therefore that no contrast can arise from it.

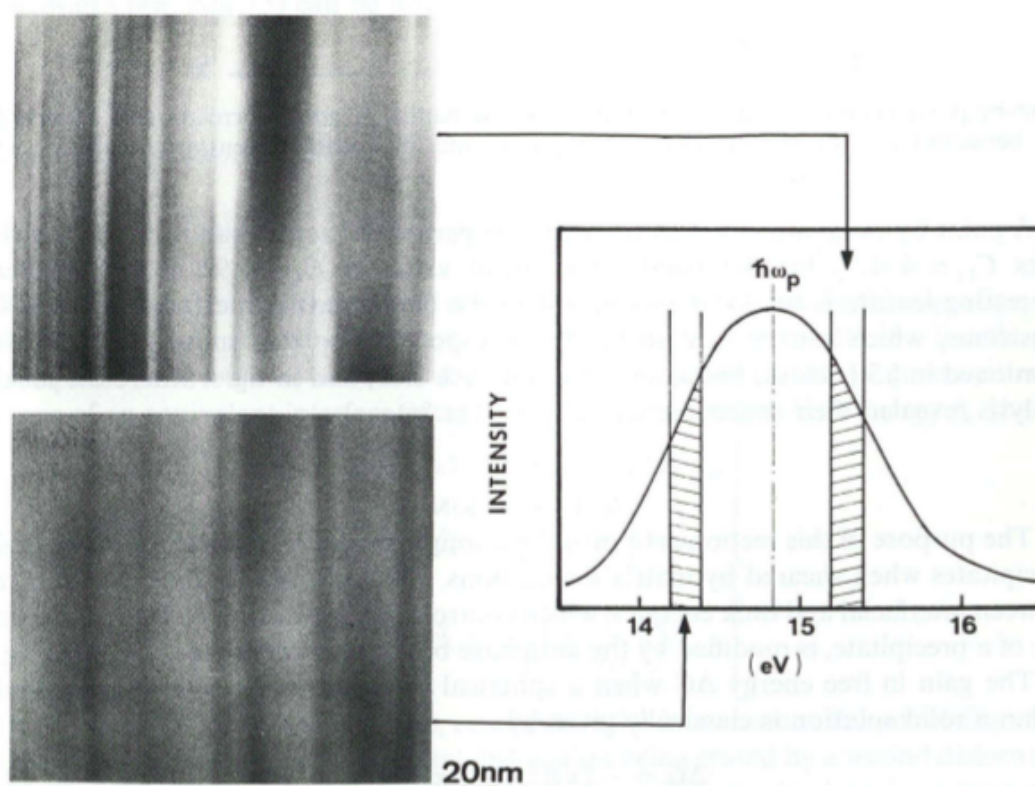
3.2.2. Lithium concentration within bands by EELS

Determination of the lithium concentration within bands by EELS must be performed in thin areas of the specimen. Indeed, bands are narrow and the enlargement of the electron beam inside the material, proportional to $t^{3/2}$ (t being the local thickness of the analysed region (Goldstein 1979)), should lead to an overlap of the beam with the matrix outside the band if t is too large. A simple calculation deriving the maximum thickness t_{\max} above which the matrix outside the band is necessarily overlapped by the electron beam gives $t_{\max} = 107$ nm, for a 1 nm probe size, a parallel incident beam and a band width of 10 nm. The conical shape of the incident and collected beams in the STEM in the operating conditions reduces t_{\max} to 72 nm. This value indicates that the determination of C_{Li} within bands should be made in the thinnest part of the foil. For the same reason, bands must be set parallel to the electron beam, which necessitates an accurate orientation of the sample, using Kikuchi patterns. This can be done only in parts of the foil thicker than the regions where the chemical analysis of the bands is achieved by EELS. This procedure means that we have followed bands from the edge of the foil toward thicker regions through the same grain, and discarded bent regions too close to the edge of the foil.

The linear variation of the plasmon energy loss ΔE against Li concentration (eqn. (1)) was used to image Li-rich regions by getting rid of thickness variations in the following way. Two energy windows at 14.3 ± 0.1 eV and 15.3 ± 0.1 eV were positioned on each side of the plasmon peak, corresponding respectively to a positive and negative slope of the function $N(E)$ which merely represents the experimental EELS spectrum. Filtered images were obtained by collecting electrons from only one energy window or from the other. Comparison of the two filtered images then provides information on eventual Li concentration fluctuations by considering the change of contrast between these two images: indeed, a variation in thickness results in a decrease or an increase in the intensity of the plasmon peak, without lateral shift, leading to a similar contrast of this region in both images, whereas a variation of Li concentration gives rise to a reversed contrast since the chemical lateral shift of the plasmon peak is accompanied by an enhancement of the number of electrons in one energy window and a simultaneous decrease of the number of electrons in the other energy window. This method enables the display of regions of different Li concentration with a better contrast than with a single energy window located at the maximum of the plasmon peak, at about 14.7 eV.

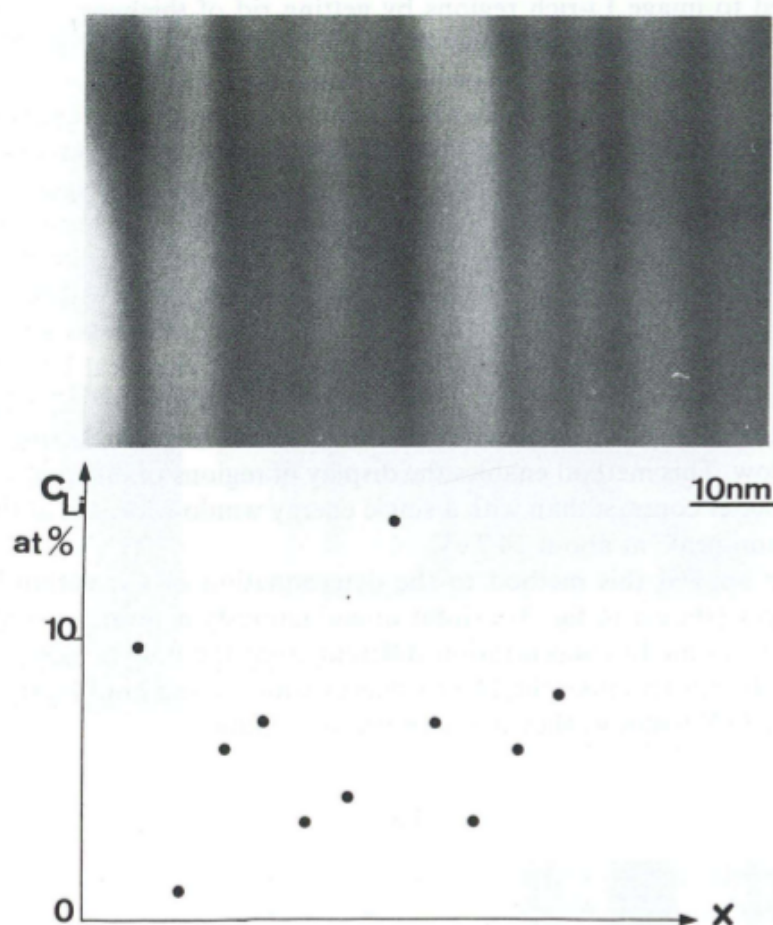
We have applied this method to the determination of C_{Li} within bands. Both filtered images (shown in fig. 3) exhibit unambiguously a reversed contrast. Bands therefore possess an Li concentration different from the matrix. Since they appear darker than the matrix under the 14.3 eV energy window and brighter than the matrix under the 15.3 eV window, they are deprived of lithium.

Fig. 3



Filtered images of PFBs obtained by EELS in the STEM using two energy windows on both sides of the plasmon peak. Reversed contrast due to Li depletion within bands (see text).

Fig. 4



Point-by-point chemical analysis of lithium across bands. A good correlation is observed between the bands (bright on the micrograph) and the lowest concentration values.

A point-by-point analysis was subsequently performed across bands (fig. 4), which gives $C_{Li} \approx 4$ at.% for the bands. The mean value of C_{Li} is 9.8 at.%. Another interesting feature is the local enrichment in the band-matrix interfaces over a few ångströms, which can be seen in fig. 3, corresponding to the 'snowdrift' contrast mentioned in § 3.1, bands being 'outlined' on each side, and in fig. 4 where the local analysis revealed their concentration ($C_{Li} \approx 12$ at.%).

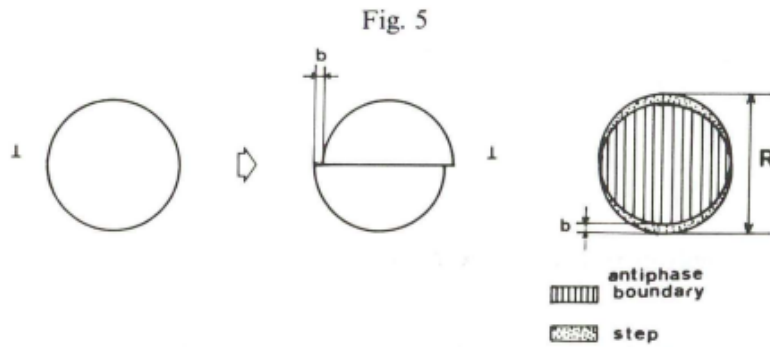
§ 4. DISCUSSION

The purpose of this section is to propose a simple model of dissolution of ordered precipitates when sheared by matrix dislocations. The basic idea is that the balance between interfacial and bulk energies, which controls the dissolution or the increase in size of a precipitate, is modified by the antiphase boundaries introduced by shearing.

The gain in free energy ΔG when a spherical precipitate of radius R is created within a solid solution is classically given by

$$\Delta G = -\frac{4}{3}\pi R^3\gamma_v + 4\pi R^2\gamma_s, \quad (2)$$

where γ_v is the gain of energy per unit volume and γ_s the interfacial energy. A critical radius R_{c0} can be defined by $(\partial\Delta G/\partial R) = 0$ or $R_{c0} = 2\gamma_s/\gamma_v$ above which the volume



Precipitate shearing: step and antiphase boundary formation.

contribution dominates and the precipitate tends to increase in size, and below which the surface term dominates, which leads to the dissolution of the precipitate.

Now, if we consider the stability of ordered precipitates (like δ') when sheared by dislocations, additional terms must be introduced in the energy balance. When a dislocation shears a precipitate (fig. 5) it creates an antiphase boundary (energy γ_a on an average surface $\frac{2}{3}\pi R^2$) and a step on the interfaces (energy γ_s on an average surface $\frac{1}{4}\pi^2 Rb$). These two terms have to be weighted by the number of shearing events. Figure 6 shows that the number dn of dislocations which can shear the precipitate during time dt can be written as

$$dn = \rho V dt. 2R, \quad (3)$$

where ρ is the mobile dislocation density and V their average velocity. Using Orowan's law, eqn. (3) can be integrated, which leads to

$$n = \frac{2R}{b} \varepsilon. \quad (4)$$

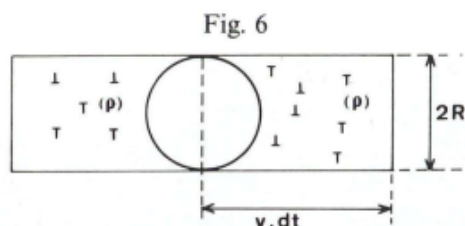
The new expression for ΔG is then

$$\Delta G = -\frac{4}{3}\pi R^3 \gamma_v + 4\pi R^2 \gamma_s + \frac{1}{2}\pi^2 R^2 \varepsilon \gamma_s + \frac{4}{3}\pi R^3 \frac{\varepsilon}{b} \gamma_a. \quad (5)$$

The antiphase term has the same R dependence as the bulk term. In this equation, the third term (step contribution) can be neglected compared with the fourth one (antiphase contribution) since $b \ll R$ and $\gamma_s \ll \gamma_a$. Therefore $\Delta G(R, \varepsilon)$ can be written in terms of an equivalent interface energy $\tilde{\gamma}_s$ and of an equivalent bulk energy $\tilde{\gamma}_v$; that is,

$$\left. \begin{aligned} \Delta G(R, \varepsilon) &= 4\pi R^2 \tilde{\gamma}_s - \frac{4}{3}\pi R^3 \tilde{\gamma}_v, \\ \tilde{\gamma}_s &= \gamma_s \left(1 + \frac{\pi \varepsilon}{8} \right) \simeq \gamma_s, \\ \tilde{\gamma}_v &= \gamma_v \left\{ 1 - \frac{a}{b \gamma_v} \varepsilon \right\}. \end{aligned} \right\} \quad (6)$$

However, in the expression of $\tilde{\gamma}_v(\varepsilon)$, one has to take into account the possibility of an antiphase boundary created by a first dislocation being erased by a second dislocation shearing the precipitate along the same glide plane. This can be done by substituting for ε an 'effective shearing strain' $\tilde{\varepsilon}$ which can be evaluated both for monotonic and cyclic straining in the following way.



Randomly distributed dislocations shearing on precipitate during dt .

In the case of a monotonic straining, if α is the probability that two dislocations emitted by the same source shear the precipitate along the same plane, we can write the number of antiphase boundaries as

$$\frac{2R}{b} (d\tilde{\varepsilon} + \tilde{\varepsilon}) = \frac{2R}{b} \tilde{\varepsilon} + \frac{2R}{b} \varepsilon (1 - \alpha\tilde{\varepsilon}) - \frac{2R}{b} \alpha\tilde{\varepsilon} d\varepsilon, \quad (7)$$

where the first term on the right accounts for the dislocations which have already sheared the precipitate, the second term for the new dislocations which shear it along planes which are still free from any antiphase boundary, and the third term for the new dislocations which shear the precipitate along pre-existing antiphase boundaries and therefore erase them. This equation leads to

$$d\varepsilon = \frac{d\tilde{\varepsilon}}{1 - 2\alpha\tilde{\varepsilon}}, \quad (8)$$

or

$$\tilde{\varepsilon} = \frac{1}{2\alpha} [1 - \exp(-2\alpha\varepsilon)]. \quad (9)$$

In the case of a cyclic straining a similar calculation would lead to

$$\tilde{\varepsilon}_N = \frac{1}{2\alpha} \{1 - \exp(-N)[1 - \exp(-2\alpha\Delta\varepsilon)]\} \quad (10)$$

where $2N$ is the number of cycles and $\Delta\varepsilon$ the plastic strain amplitude. The expressions for $\tilde{\varepsilon}$ given by eqns. (9) and (10) must be used instead of ε in eqns. (6).

From eqns. (6), the critical radius of redissolution \tilde{R}_C can be written as

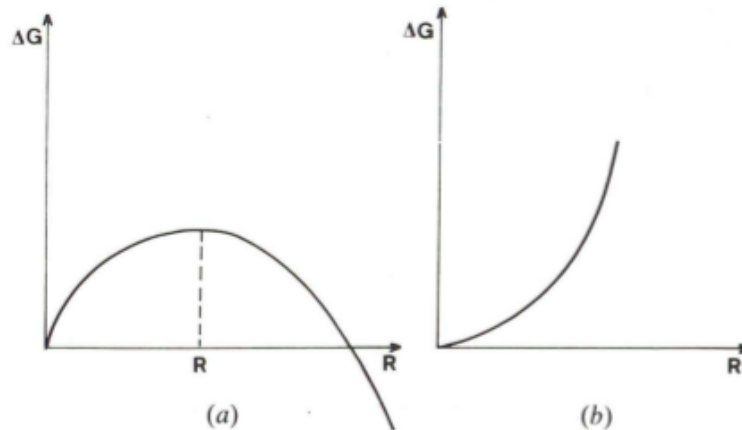
$$\tilde{R}_C(\varepsilon) = R_{C_0} \left(\frac{1 + \pi\tilde{\varepsilon}/8}{1 - \tilde{\varepsilon}/\tilde{\varepsilon}_C} \right). \quad (11)$$

where $\tilde{\varepsilon}_C$ is the critical value of $\tilde{\varepsilon}$ for which $\gamma_v(\tilde{\varepsilon})$ becomes zero; that is,

$$\tilde{\varepsilon}_C = b \frac{\gamma_v}{\gamma_a} \quad (12)$$

For low strains ($\tilde{\varepsilon} < \tilde{\varepsilon}_C$) the ΔG against R curve has the usual shape with a saddle point at $R = R_C$ (fig. 7(a)). Precipitates with radius $R > \tilde{R}_C(\tilde{\varepsilon})$ do not dissolve. But when the strain $\tilde{\varepsilon}$ reaches $\tilde{\varepsilon}_C$, \tilde{R}_C becomes infinite. This means that for large strains $\Delta G(R)$ is an increasing function of R (fig. 7(b)); there is no saddle point and all the precipitates, even the larger ones, should dissolve. In Al-Li alloys an estimation of $\tilde{\varepsilon}$ taking $R_{C_0} = 2b$, $\gamma_a = 150 \text{ mJ m}^{-2}$ and $\gamma_s = 25 \text{ mJ m}^{-2}$ (Sainfort 1985, Livet and Bloch 1985) gives $\tilde{\varepsilon}_C = 20\%$. Although such a strain can hardly be reached by

Fig. 7



Free energy of a precipitate as a function of its size. \bar{R}_c is the critical size of redissolution. The shape of the curve changes drastically at $\bar{\epsilon} = \bar{\epsilon}_c$: (a) $\bar{\epsilon} < \bar{\epsilon}_c$; (b) $\bar{\epsilon} \geq \bar{\epsilon}_c$.

monotonic deformation, a cumulative 'effective' deformation of 20% is likely to be locally reached in fatigue.

The morphology of the precipitate free bands and some results concerning their spacing or width can be derived from this model.

The basic idea is the following. Fatigue produces vacancies and interstitials which enhance the coarsening kinetics in a Lifschitz-Slyosov-Wagner regime, and this tends to increase the average radius of precipitates.

On the other side, the critical radius of dissolution R_c increases with the cumulative strain, and such a mechanism tends to dissolve more and more precipitates. Moreover, the shearing of precipitates is a destabilizing process in plastic deformation: the more a precipitate is sheared, the more easily it will be sheared again, since its size in the glide plane decreases at every shearing event. This mechanism leads to a localization of deformation, which can be described by a characteristic length λ , as shown in fig. 8(b). This localization of plastic deformation produces a spatial inhomogeneity both in the coarsening kinetics and in the redissolution process. The precipitate-free bands arise from the competition between the two phenomena mentioned above, and from the coupling between plastic localization and redissolution.

Three main problems can be solved by this approach:

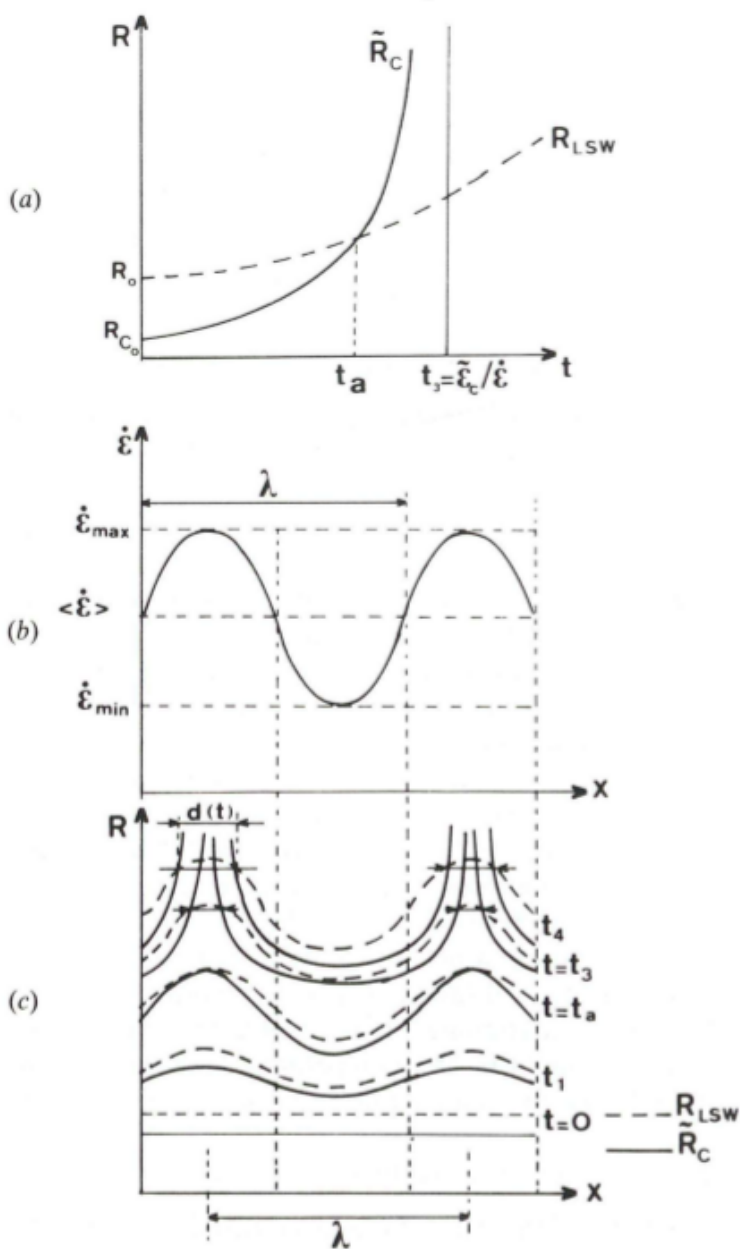
- (1) What is the width of the bands for a given length of localization?
- (2) What is the effect of strain gradients on the size repartition of precipitates outside the band?
- (3) What happens to the lithium thrown back into solid solution?

For the sake of simplicity, we shall assume that Li diffusion is mainly due to vacancies, and we shall neglect divacancies and other more complicated defects in the evolution of the density of vacancies C .

To answer these three questions one must first derive the equation of evolution for the vacancy density resulting from strain localization. In the following, all variables are local and the spatial average values will be labelled $\langle \rangle$.

The vacancy production rate induced by strain is usually taken equal to $k\dot{\epsilon}$ (Mecking and Estrin 1980). The order of magnitude of k is 10^{-4} .

Fig. 8



(a) Variations with strain (or with time at constant strain rate $\dot{\epsilon}$) of the critical radius of redissolution \tilde{R}_C (full line) and of the coalescence radius R_{LSW} (dashed line). For times $t > t_a$, precipitates become unstable. (b) Strain-rate localization, characterized by a wavelength λ , and arising from precipitate shearing. (c) Critical radius of redissolution $\tilde{R}_C(x, t)$ (full lines) and coalescence radius $R_{LSW}(x, t)$ (dashed lines).

For $0 < t < t_a$: $R_{LSW} > \tilde{R}_C$ everywhere. Precipitates are stable.

For $t = t_a$: $R_{LSW} = \tilde{R}_C$ for $x = x_M + n\lambda$ where $\dot{\epsilon}(x)$ is maximum.

For $t_a < t$: a channel of width $d(t)$ opens, where precipitates are unstable.

For $t = \tilde{\epsilon}_c / \dot{\epsilon}$: \tilde{R}_C becomes infinite at $x = x + n\lambda$, i.e. at the centre of the channels.

The vacancy concentration C tends to relax to its thermodynamical equilibrium value \bar{C} with a time constant τ . Actually, the kinetics of relaxation have been shown to be rather in $\exp[-(t/t_0)^{1/2}]$ (Wintenberger 1959); but we consider essentially steady-state regimes, and with a suitable value of τ it can be approached by $\partial C/\partial t = (C - \bar{C})/\tau$. The order of magnitude of τ is between 1 and 10 seconds.

The equation ruling the evolution of C is then

$$\frac{\partial C}{\partial t} = -\frac{C - \bar{C}}{\tau} + k\dot{\epsilon}(x, t) + D_0 \frac{\partial^2 C}{\partial X^2}, \quad (13)$$

where D_0 is the diffusion coefficient of vacancies.

$\Lambda = (D_0 \tau)^{1/2}$ is a characteristic length of the problem: its order of magnitude is 10^{-7} m. The other characteristic length is λ , the length of localization (fig. 8(b)). $\dot{\epsilon}$ is given by

$$\dot{\epsilon}(x) = \langle \dot{\epsilon} \rangle + \dot{E} \sin(2\pi x/\lambda). \quad (14)$$

Equations (14) and (13) have a steady-state solution $\tilde{C}(x)$ given by

$$\tilde{C}(x) = \bar{C} + k \frac{(\dot{\epsilon})\Lambda^2}{D_0} + \frac{k}{D_0} [\dot{\epsilon}(x) - \langle \dot{\epsilon} \rangle] \left(\frac{\Lambda}{\lambda} \right) \left(\frac{\Lambda^2 \lambda^2}{\lambda^2 + \Lambda^2} \right). \quad (15)$$

Thus, \tilde{C} oscillates in phase with $\dot{\epsilon}(x)$. The characteristic time to reach this steady state is τ .

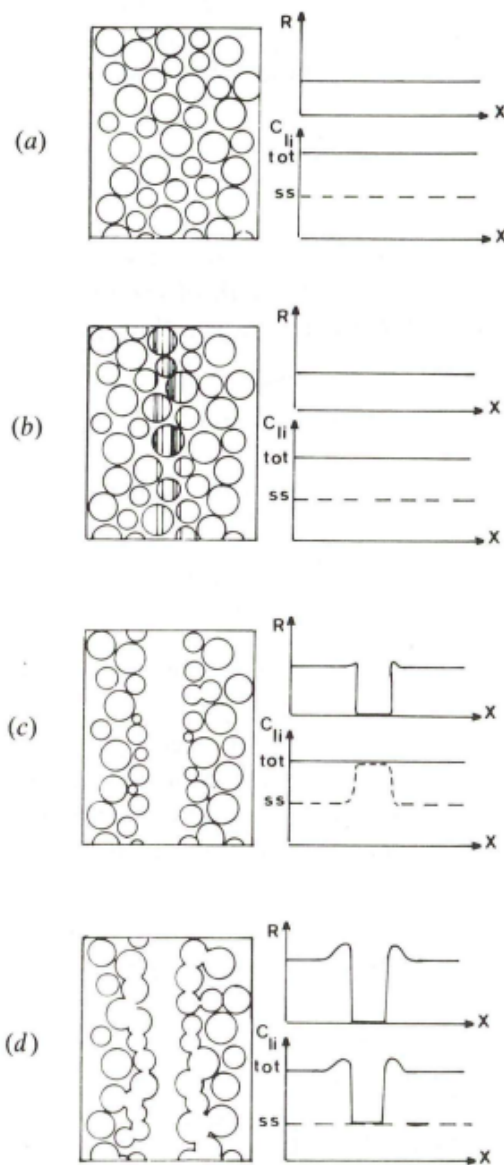
The condition of redissolution is obtained by writing that the precipitate radius given by the LSW law is overshoot by the critical radius \tilde{R}_C for redissolution, as shown in fig. 8(a). For a given strain rate this condition is realized after a time t_a smaller than the time $\tilde{\epsilon}_c/\dot{\epsilon}$ for which \tilde{R}_C becomes infinite. The time t_a is the solution of the equation

$$\begin{aligned} R_{LSW}^3(t) &= R_0^3 + KD_{Li} \frac{\langle C \rangle}{\bar{C}} \left[1 + \left(\frac{k}{D_0 \langle C \rangle} \right) \left(\frac{\Lambda}{\lambda} \right) \left(\frac{\Lambda^2 \lambda^2}{\Lambda^2 + \lambda^2} \right) (\dot{\epsilon} - \langle \dot{\epsilon} \rangle) \right] t \\ &= R_{C_0}^3 \left[\frac{1 + \frac{\pi^2}{8} \tilde{\epsilon}(t)}{1 - \frac{\tilde{\epsilon}(t)}{\tilde{\epsilon}_c}} \right]^3 = \tilde{R}_C^3(t), \end{aligned} \quad (16)$$

D_{Li} being the diffusion coefficient of Li at room temperature without cyclic straining, and K the LSW coefficient. $\tilde{\epsilon}$ is given by eqn. (10) and can be approximated by $\tilde{\epsilon} \sim \dot{\epsilon}t$. This approximation can be supported by the fact that, R being small, t_a is much smaller than $1/\langle \dot{\epsilon} \rangle$.

Because of the strain localization mentioned above, $\dot{\epsilon}$ is a function of x as schematized by eqn. (14) and fig. 8(b), and the realization of condition (16) will occur at different places for different times. Figure 8(c) shows the variation of R_{LSW} and R_C with x for increasing times. At the beginning (time t_1 for instance) R_{LSW} is larger than R_C everywhere (failing which no precipitates could be observed before straining). For $t = t_a$, \tilde{R}_C overshoots R_{LSW} at places where $\dot{\epsilon}$ is maximum. For times larger than t_a a channel of increasing width $d(t)$ open within which precipitates are unstable and

Fig. 9



- (a) Initial state of δ' precipitation before fatigue; both the average radius of precipitates R , and Li concentration in δ' and solid solution (total, in full line) or only in solid solution (ss, in dashed line) are homogeneous. (b) First stages of precipitates shearing and antiphase boundaries formation. (c) Precipitates become unstable and dissolve in the matrix leading to a local increase in solid-solution lithium concentration. (d) The lithium concentration is solid solution created in (c) leads to intense lithium diffusion helped by fatigue-induced vacancies, and Li reprecipitates on the side of the band, (snowplough effect). The result is a permanent gradient of the total concentration of lithium (full line).

dissolve. This gives the precipitation-free bands described above. From eqn. (16), taking $\tilde{\varepsilon} \sim \dot{\varepsilon}t$ and $\langle C \rangle / \bar{C} \gg 1$, one can show that

$$t_a = \frac{\tilde{\varepsilon}_C}{\varepsilon_{\max}} \left[\left(\frac{R_0}{R_{C_0}} \right)^3 - 1 \right] \quad (17)$$

and

$$\frac{d(t)}{\lambda} = \frac{1}{\pi\sqrt{2}} \left(1 - \frac{t_a}{t} \right)^{1/2}. \quad (18)$$

Equation (18) shows that $d = 0$ for $t = t_a$ (fig. 8(c)), and for $t \gg t_a$ one gets $d/\lambda = 0.22$. This order of magnitude of d/λ is in fairly good agreement with observation (see fig. 1(a)) which gives $d/\lambda = 0.185$. A reasonable value of t_a is between 10 and 100 seconds (if one takes $\dot{\varepsilon}_{\max}/\langle \dot{\varepsilon} \rangle$ between 10 and 100 as in copper).

One can then explain the general morphology of the precipitate-free bands at the saturation state (see fig. 9). The scenario is the following. Precipitates are locally sheared (fig. 9(b)) and, when sufficiently sheared, they dissolve (fig. 9(c)). The widths of the channels increase and more and more lithium is thrown into solid solution. Locally (in the band), the solid solution is enriched in Li (fig. 9(c)). This lithium diffuses (fig. 9(d)), reprecipitates on the sides of the bands, where the volume fraction of δ' increases and where enhanced coarsening takes place: this is the reason why the 'snowplough effect' takes place.

When Li has diffused in order to homogenize the solid solution, because of the absence of δ' precipitates, the inner bands are depleted in lithium under the phase diagram limit; even when cycling has stopped, they remain depleted, leading to the experimentally observed gradient in lithium concentration.

§ 5. CONCLUSIONS

We have shown that small ordered and shearable δ' precipitates in an Al-2.5wt%Li alloy were responsible for a strong strain localization. The associated microstructure consisted of narrow channels parallel to $\{111\}$ slip planes and free from precipitates (precipitate-free bands or PFBs), in which dislocations could move much more easily than outside the bands. A local chemical analysis of EELS showed that they are also depleted of Li. The model proposed for this mechanism is a kind of phase transition induced by plastic strain: the additional energy coming from antiphase boundaries created by shearing leads to a redissolution of precipitates. The ratio of the band width to the band separation deduced from the model is in reasonable agreement with experimental results.

This model could be applied to other materials. In particular an experimental investigation of the influence of the stacking fault and antiphase boundary energies on precipitate redissolution should be of interest, since a stronger localization of plastic deformation can reduce drastically the fatigue life of a material.

ACKNOWLEDGMENTS

The authors thank Cegedur Pechiney Research Center for providing the specimens and financial assistance for fatigue tests; Pechiney for financial support of one of us (Y. Bréchet); Dr B. Wack and Dr S. Han for mechanical testing of specimens; and Dr Livet for X-ray low-angle scattering experiments.

REFERENCES

- BRECHET, Y., GUYOT, P., and LOUCHET, F., 1986, *Proceedings of the International Conference on Aluminium Alloys*, Charlottesville.
- CALABRESE, C., and LAIRD, C., 1977, *Mater. Sci. Engng.*, **13**, 141.
- FOUGERES, R., GENTZBITTEL, and VIGIER, 1987, *J. Phys., Paris* (to be published).
- GOLDSTEIN, J. L., 1979, *Introduction to Analytical Electron Microscopy*, edited by J. J. Mren, J. I. Goldstein and D. C. Joy (New York: Plenum Press), p. 101.
- HAN, S., and WACK, B., 1987, *Proceedings of the Fourth International Conference on Al-Li Alloys, Paris* (to be published in *J. Phys., Paris Colloq.*).
- KÖHLER, E., BISCHOFF, E., and GEROLD, V., 1984, *Scripta metall.*, **18**, 699.
- LIVET, F., and BLOCH, D., 1985, *Scripta metall.*, **19**, 1147.
- MAGNIN, T., DRIVER, J., LEPINOUX, J., and KUBIN, L. P., 1984, *Rev. Phys. Appl.*, **19**, 467.
- MECKING, H., and ESTRIN, Y., 1980, *Scripta metall.*, **14**, 815.
- MUGHRABI, H., 1985, *Proceedings of the Seventh International Conference on the Strength of Metals and Alloys*, Montreal, Vol. 3 (Oxford: Pergamon Press), p. 1917.
- SAINFORT, P., 1985, Ph.D. Thesis, Grenoble University.
- SAINFORT, P., and GUYOT, P., 1985a, *Proceedings of the Seventh International Conference on the Strength of Metals and Alloys*, Montreal, Vol. 1 (Oxford: Pergamon Press), p. 441; 1985 b, *Phil. Mag. A*, **51**, 575.
- VOGEL, W., WILHEM, M., and GEROLD, V., 1979, *Proceedings of the Seventh International Conference on the Strength of Metals and Alloys*, Aachen, Vol. 2 (Oxford: Pergamon Press), p. 1175.
- WINTENBERGER, M., 1959, *Acta metall.*, **7**, 549.